communications chemistry

A Nature Portfolio journal

Article

https://doi.org/10.1038/s42004-025-01790-x

Insights into proton transfer dynamics in histidine tautomers of amyloid-β (1-40)

Yingqi Tang[1,5], Yoshifumi Nishimura[2,5], Nannan Li[1], Hai Li[1], Abbas Salimi[1], Kensuke Ishida[3], Aditya Wibawa Sakti[3,4] ✉, Hiromi Nakai[2,3] ✉, Rakesh Parida[1] ✉ & Jin Yong Lee[1] ✉

Histidine tautomerization within amyloid beta (Aβ) peptides is crucial in understanding the molecular mechanisms underlying Alzheimer's disease and its potential therapeutic strategies. Despite its significance, the proton transfer dynamics between histidine residues in Aβ-40 at the protein level remain insufficiently explored due to the complexity of solvent effects and the computational challenges of large-scale simulations. This study conducted fully quantum mechanical molecular dynamics (QM-MD) simulations coupled with metadynamics (MTD) to investigate the tautomerization process between histidine tautomers in Aβ-40 within an aqueous environment. Using the divide-and-conquer density-functional tight-binding (DC-DFTB) method, a system of ~3000 atoms was modeled to capture the atomic-scale interactions. MTD simulations revealed that water molecules mediate the tautomerization of histidine residues, HIS 13 and HIS 14, stabilizing specific tautomeric forms. The two-dimensional well-tempered MTD (2D WTMTD) results identified a reaction barrier of approximately 3.51 kcal mol^{-1} for tautomerization. This study represents the first comprehensive QM-MD/MTD investigation of histidine tautomerization in amyloid beta peptides, offering insights into the tautomerization process.

According to statistics from the World Health Organization (WHO), the number of dementia patients worldwide will be estimated to exceed 100 million in 2050[1]. Alzheimer's disease (AD), one of the leading causes of dementia, presents significant challenges both medically and financially for families and society[2]. In recent decades, extensive research has been conducted to explore the underlying mechanisms of AD, with various hypotheses which include the cholinergic, metal, oxidative stress, and tautomerism hypotheses[3–9]. Chelation therapy has been widely investigated as a means of restoring metal ion balance in the brain, since chelators can sequester and stabilize excess metal ions through the formation of multiple coordination bonds[10]. Among the different scaffolds tested, natural and synthetic coumarin derivatives have drawn particular interest[10,11]. Owing to their versatile biological activity, including inhibition of cholinesterases (ChEs) and monoamine oxidase B (MAO-B), depending on the substitution pattern, coumarins are now considered a privileged framework for the design of multitarget ligands in AD therapy[12].

Parallel to this, growing evidence indicates that soluble Aβ dimers, rather than mature fibrils, represent the most neurotoxic species in AD[13,14]. Their formation is governed by specific electrostatic and hydrophobic contacts between key residues: for example, Arg5 interacts with negatively charged partners, while Lys28 forms stabilizing salt bridges with Glu22 and Asp23[12]. Hydrophobic residues, including Ile31, Leu34, Met35, Val36, and Val40 further enhance β-sheet stacking and aggregation[15,16]. External modulators such as metal ions (e.g., Cu^{2+}, Zn^{2+}) can shift these assemblies toward alternative conformations[17]. Importantly, the existence of Aβ dimers has been confirmed in patient brain samples using advanced methods such as single-molecule force microscopy (SMFS) and mass spectrometry, underscoring their contribution to synaptic dysfunction and highlighting them as promising therapeutic targets[13,18,19].

Among these, the tautomerism hypothesis has gained significant recognition, suggesting that the aggregation and accumulation of β-amyloid plaques play a key role in both bio-pathological models and clinical AD patients[8,9]. Researchers have reported that the aggregation of amyloid peptides is affected by temperature, metal ions, pH, and histidine tautomerization etc[20–23]. However, limited research has focused on understanding the mechanisms behind amyloid aggregation. The tautomer hypothesis has been introduced as a potential explanation[24,25], suggesting that the tautomeric state of the imidazole ring in histidine is pivotal to Aβ misfolding. All

[1]Department of Chemistry, Sungkyunkwan University, Suwon, South Korea. [2]Waseda Research Institute for Science and Engineering, Waseda University, Tokyo, Japan. [3]Department of Chemistry and Biochemistry, School of Advanced Science and Engineering, Waseda University, Tokyo, Japan. [4]Global Center for Science and Engineering, Waseda University, Tokyo, Japan. [5]These authors contributed equally: Yingqi Tang, Yoshifumi Nishimura.
✉e-mail: aditya@aoni.waseda.jp; nakai@waseda.jp; rakeshparida92@gmail.com; jinylee@skku.edu

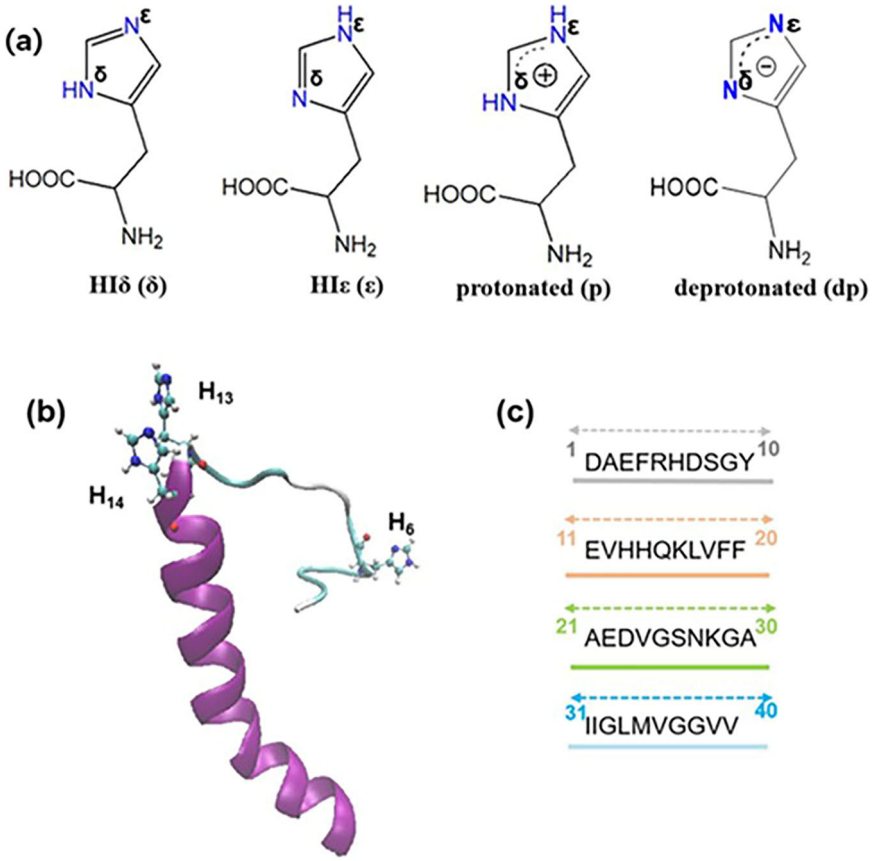

Fig. 1 | Schematic representation of histidine and Aβ-40 structures. a The Chemical structures of monoprotonated (δ and ε), fully protonated (p), and deprotonated (dp) forms of histidine, **b** the initial structure of Aβ-40 protein, and **c** the amino acid sequence of Aβ-40 protein.

the tautomeric forms of histidine are illustrated in Fig. 1. The Aβ-40 is one of the major amyloid proteins in the accumulation of amyloid peptide plaques, so it garnered significant attention from neuroscience researchers[26–28].

To unravel the pathogenesis of Alzheimer's disease and advance therapeutic approaches, Our group employed molecular dynamics simulations to investigate the effects of histidine tautomerism on Aβ-40 monomers, homodimers, and pentamers[25–29]. In one of our earlier studies, we explored the synergistic influence of histidine tautomerism and its interactions with Au(111) surfaces, using a combination of molecular dynamics simulations and two-dimensional infrared spectroscopy[30]. This integrative approach provided valuable insights into how intrinsic tautomeric switching, together with external environmental factors such as metallic surfaces, can modulate amyloid misfolding pathways relevant to Alzheimer's disease. Additionally, quantum mechanical calculations were employed to investigate the role of 3–5 water molecules in facilitating proton transfer during histidine tautomerization, although these studies were limited to the amino acid level, specifically focusing on the δ and ε tautomers[31]. A more comprehensive understanding of the tautomer hypothesis requires a deeper investigation into proton transfer dynamics within peptides and water molecules. Understanding the proton transfer mechanism of histidine tautomers in Aβ-40 protein is important for elucidating the origin of Aβ aggregation. Several studies have emphasized the critical role of the tautomeric states of histidine residues 6, 13, and 14 in Aβ-40 in influencing amyloid-peptide aggregation[26–28,32]. However, the mechanism of the proton transfer in histidine tautomers within the tautomerism hypothesis has been inadequately explored, primarily due to the technical constraints in clinical diagnostics and the difficulty of theoretical studies. Moreover, the modeling systems containing excess protons and solvated protein are not feasible to simulate at the DFT level due to their large number of atoms.

Recently, Nakai et al. employed the divide-and-conquer density-functional tight-binding (DC-DFTB) method to investigate rare events in large biomolecular systems, specifically studying the proton transfer mechanism from the retinal Schiff base to Asp85 in bacteriorhodopsin (BR) using models containing ~3750 atoms[33]. Their work demonstrated the remarkable efficiency of DC-DFTB calculations with the $D_{CDFTBMD}$ program, particularly for large-scale systems, facilitating quantum mechanical (QM) simulations[34–36]. Given the strengths of the $D_{CDFTBMD}$ program in simulating proton transfer within large protein systems[33,35–37], we employed molecular dynamics and metadynamics simulations in this study to investigate the tautomerization process of histidine in the Aβ-40 protein.

Water molecules are well-known to facilitate the tautomerization reactions via proton transfer mechanism in biological systems[31,38,39], making it crucial to explore this process within histidine tautomers of Aβ-40 in aqueous environments. Given the close proximity of residues HIS13 and HIS14 in Aβ40, this region is especially conducive to proton transfer. Although the proton transfer barrier typically exceeds thermal fluctuations, preventing full capture of transition states in unbiased molecular dynamics simulations, enhanced sampling techniques like metadynamics and umbrella sampling have proven effective[40,41]. These methods allow for the precise estimation of proton transfer barriers by reconstructing the free energy surface and statistically analyzing the transition states of these rare events.

In this study, we employed metadynamics simulations at the DC-DFTB level to get insight into the proton transfer phenomena between two histidine tautomers within the Aβ-40 peptide. We examined the proton transfer dynamics by analyzing the radial distribution function, the constructed free energy surfaces, and Mulliken charges associated with the tautomers. This study offers an insights into the mechanisms that may underpin Aβ aggregation in Alzheimer's disease and represents a significant advancement in supporting the histidine tautomerism hypothesis in biochemical research.

Results and discussion

Structural evolution from MD simulation

The snapshots of the initial and simulated geometries of all isomers of Aβ-40 obtained at the end of the four different simulations are displayed in Fig. 2

The simulated structure shows that the $\delta\delta$ tautomer has some β-sheet characteristics, a key element in amyloid aggregation. However, this was initially based on visual inspection of the snapshots. To confirm our observation, we calculated the average α-helix and β-sheet content for all isomers, with the results summarized in Supplementary Table 1.

Supplementary Table 1 indicates that 10% of the $\delta\delta$ tautomer adopts a β-sheet structure. Detailed insights into the secondary structure changes throughout the simulation are provided through the Defined Secondary Structure of Proteins (DSSP) analysis, as shown in Supplementary Fig. 1. Notably, the β-sheet structures in the $\delta\delta$ tautomer are localized at the Arg5-His6 and Gly38-Val39 residues. This β-sheet-rich conformation is known to be highly toxic in amyloid proteins[42–44]. Therefore, the $\delta\delta$ tautomer of Aβ-40 was selected for further calculations and deeper investigation in this study.

The protein backbone's root mean square deviation (RMSD), shown in Supplementary Fig. 2a, confirms that the system is well-equilibrated. Further calculations were performed to investigate the role of water molecules around the imidazole ring, specifically focusing on $N_{\delta/\varepsilon}H$ (H atom connected to $N_{\delta/\varepsilon}$) and $N_{\delta/\varepsilon}$ atoms. This was done by calculating the pair distribution function between the O/H atoms of water molecules and the $N_{\delta/\varepsilon}H$ and $N_{\delta/\varepsilon}$ atoms, respectively, as these atoms play a key role in the tautomerization reaction in Aβ-40 protein. The resulting plot is provided in Supplementary Fig. 2b.

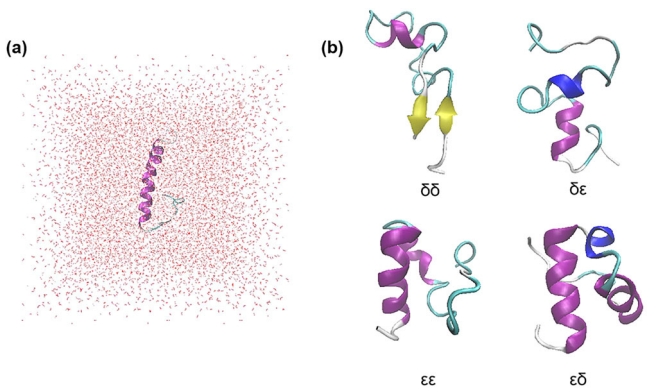

Fig. 2 | Representative structures of Aβ-40 tautomers from MD simulation. a The Schematic representation of the initial snapshot from the MD simulation, **b** the structures of Aβ-40 isomers after 200 ns simulations. Purple and yellow colors denote α-helix and β-sheets, respectively.

As shown in Supplementary Fig. 2b, the RDFs of N_δ-H in HIS13 and HIS14 residues to water O atoms display a sharp peak around 1.90 Å, indicating water molecules are close to the N_δ-H atom. The second solvation shell for HIS13 appears at 3.45-3.85 Å, while for HIS 14, it extends to 4.80 Å. Additionally, the RDF of H (from water molecule) and the N_ε atom of HIS 13 show a sharp peak at 2.30 Å and a broader second peak at 3.50–4.80 Å. These findings suggest that water molecules surrounding the HIS 13 and 14 residues at varying distances could facilitate water-mediated histidine tautomerization. In further studies, we have explained the tautomerism mechanism by adopting various techniques like DCDFTB-MD/MTD simulation, 1D/2D WTMTD, and RDF analyses.

DC-DFTB molecular dynamics

The simulated system was reduced to ~2998 atoms to optimize computational resources, as shown in Supplementary Fig. 3a. The simulated and initial coordinates of this system are provided in supplementary Data 1 and 2, respectively. The parameters for the DC method were determined through a systematic evaluation of energy dependence on grid size and buffer radius. These parameters were refined based on preliminary single-point energy calculations of the reduced system, as detailed in Supplementary Fig. 3 and further discussed in Supplementary method of the Supplementary Information. The system was equilibrated for 100 ps using DCDFTB-MD simulations, and the stability was confirmed through the energy convergence plot (see Supplementary Fig. 3c, d). To analyze the distribution of water molecules around HIS13 and HIS14, RDFs were computed between the O atoms of water molecules and the $N_\delta H$ atom of HIS13/HIS14 residues, as well as for the H atoms of water molecules and the N_ε atom of these residues. The corresponding RDFs are presented in Fig. 3.

As depicted in Fig. 3a, the RDF for the H atoms of water molecules and the N_ε atom of the HIS13 residues displays the first peak at 2.14 Å, which is similar to the RDF for the O atom in water molecules to the N_δ-H atom of the HIS13. However, the HIS14 residue shows a pronounced peak at 1.02 Å, indicating the proximity of a water molecule to the N_ε atom. This suggests that the N_ε atom in the HIS14 residue could readily abstract a proton, leading to its protonated form (p). Additional peaks at 2.22 Å and 3.17 Å correspond to the first and second solvation shells of the N_ε atom, respectively. Similarly, the RDF for the N_δ-H atom in the HIS14 residue follows a comparable pattern. These findings indicate that water molecules preferentially associate with the N_ε atom of histidine residues, particularly around the HIS14 residue.

To further investigate proton transfer in the histidine tautomers of Aβ-40, we analyzed the DCDFTB-MD simulation trajectory (Fig. 4). Supplementary Fig. 4 shows more detailed snapshots The system was equilibrated for 100 ps of the proton transfer pathway. Within 100 ps of equilibration, a proton transfer phenomenon was observed between the HIS14 residue and a water molecule. Figure 4a shows the close-up structures of HIS14 and the

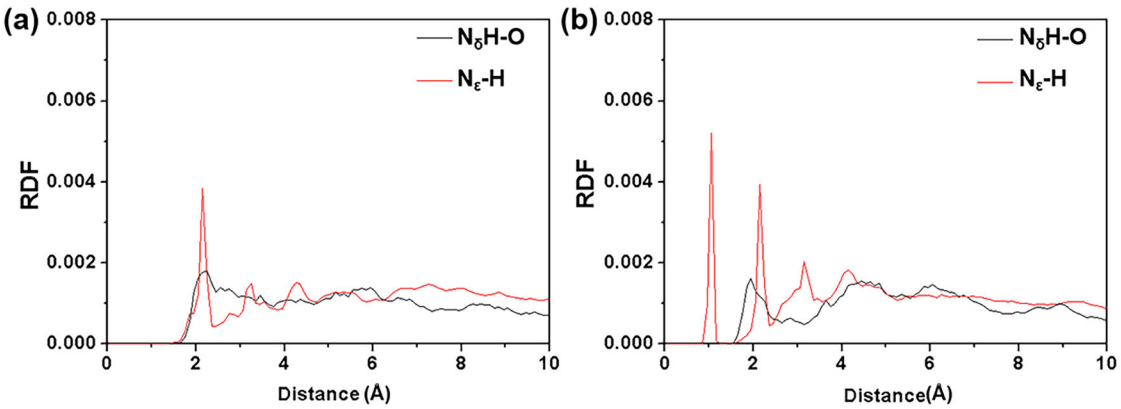

Fig. 3 | RDFs of solvent around histidine residues. a RDFs of O atoms in water molecules around the $N_\delta H$ atom in histidine residue and H atoms in water molecules around the N_ε atom in HIS13 and **b** HIS14 residues obtained from the 100 ps DC-DFTB-MD simulation, respectively.

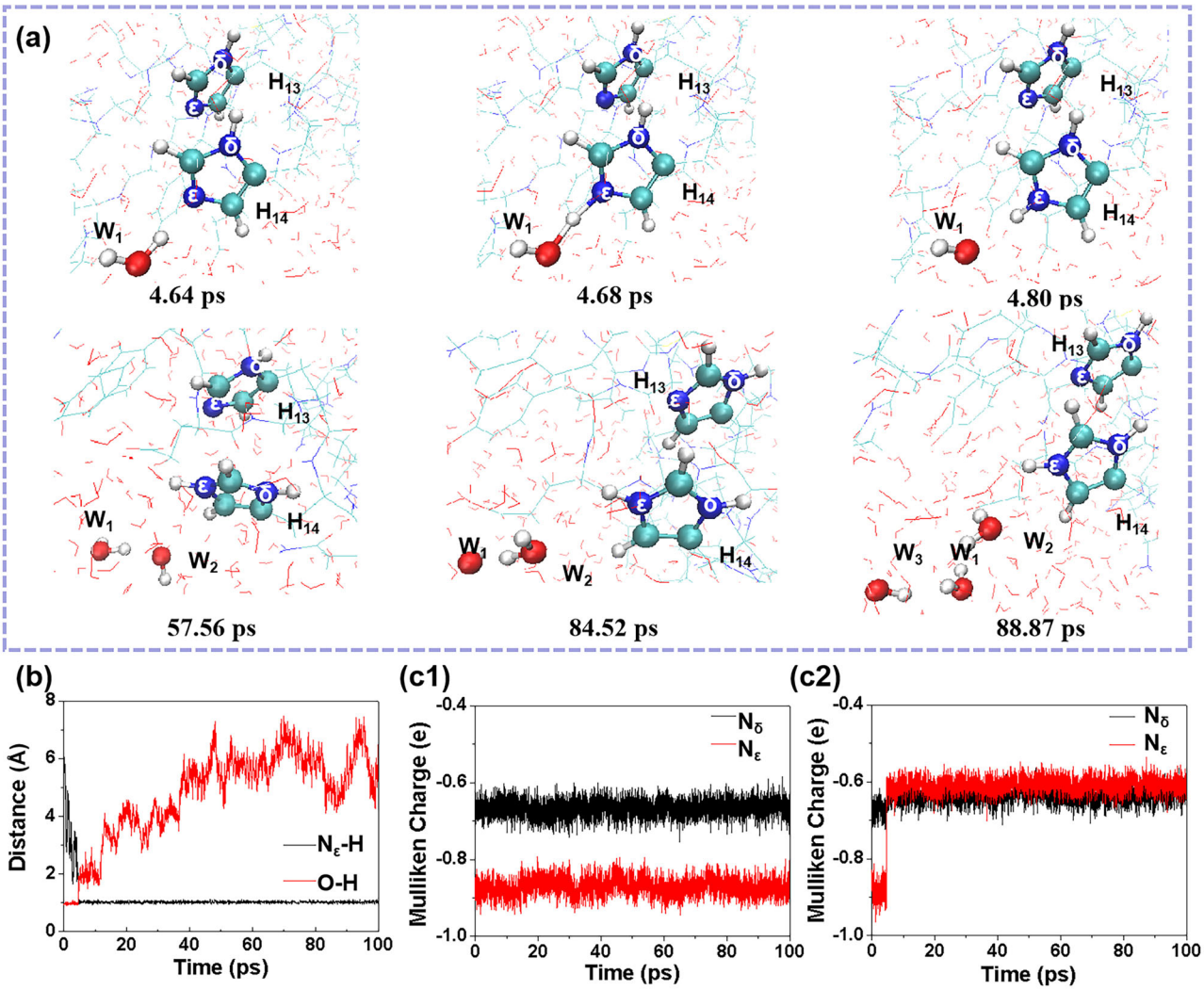

Fig. 4 | Aβ-40 tautomerization process in 100 ps DC-DFTB-MD equilibration. **a** The key close-up snapshots of the active site of HIS13 and HIS14 residues during the tautomerization obtained from 100 ps DC-DFTB-MD equilibration (H_{13} and H_{14} are used instead of HIS13 and HIS14, respectively, inside the figure). **b** Time evolution of the distances between the N_ε atom of the HIS14 residue and the H atom of the water molecule (W1), as well as between the H atom and the O atom of the water molecule, highlighting proton transfer events. Time-dependent variations in the Mulliken charges of the N_ε and N_δ atoms in the **c1** HIS13 residue and **c2** in the HIS14 residue, which refer to a change in the electronic structure associated with the tautomerization process.

interacting water molecule during the reaction. In contrast, Fig. 4b depicts the time evolution of distances between the N_ε atom of HIS14 and the water molecule's H and O atoms. Initially, the N_ε-H (H atom is from the W_1 molecule) distance was 6.04 Å, with the O-H (in the W_1 molecule) bond at 0.95 Å. At 4.68 ps, the O-H bond lengthened to 1.61 Å, and the H atom approached the N_ε atom with 1.08 Å. By 4.80 ps, the proton was transferred, forming a 1.01 Å N_ε-H bond and turning the water molecule into a hydroxide ion. After that, the proton transfer process was observed in other water molecules, which is also explained by the reason that the distance of Nε-H increases as the simulation time progresses.

Mulliken charge analysis (Fig. 4c) revealed that the charges of the N_δ and N_ε atoms in HIS13 remained unchanged, suggesting HIS13 stayed in the δ state. And, a significant change in the charge of the N_ε atom of HIS14 from −0.9 e to −0.6 |e| around 4.80 ps, indicating its protonated form. These findings confirm that after 100 ps of equilibration, Aβ-40 undergoes a tautomeric shift from the (δ, δ) form to the (δ, p) state.

Proton transfer dynamics from metadynamics (MTD) simulation

To obtain the free energy profiles for proton transfer in the Aβ-40 tautomers, we have carried out DC-DFTB-MD/MTD simulations. Considering the two-dimensional (2D) collective variable (CV) sampling can enhance the accuracy of free energy, where two CVs are simultaneously employed in the metadynamics process, allowing for more efficient capture of transition states[45–49]. Thus, to further improve the precision of the estimated activation free energy, 2D metadynamics simulations were performed. In this approach, the H coordination numbers of HIS13 and HIS14 were selected as CV1 and CV2 for free energy sampling.

The two-dimensional free energy surface (FES) based on a 100 ps 2D WTMTD trajectory for HIS13 and HIS14 residues of Aβ-40 is shown in Fig. 5a, while the corresponding coordinates of the tautomeric Aβ-40 in an aqueous environment are provided in supplementary Data 3–5. The H-coordination numbers indicate the protonation states: 2 for protonated histidine, 1 for the δ or ε form, and 0 for the deprotonated form. The minimum energy (0.00 kcal mol^{-1}) occurs at (CV1, CV2)≃(1.9, 2.0), representing the most stable (p, p) tautomer. Another local minimum appears at (1.9,1.4) with 2.30 ± 0.20 kcal mol^{-1}, where HIS14 could be in the δ or ε form. Therefore, we need to analyze the Mulliken charge values and the snapshot along the simulation to confirm the specific protonated state. A saddle point at (1.9, 1.6) with 5.81 ± 0.50 kcal mol^{-1} suggests a proton transfer barrier of 3.51 kcal mol^{-1}. The estimated free energy barrier differs from MTD results due to more frequent transition state capture in 2D WTMTD simulations. Additionally, we performed a repeatability 100 ps

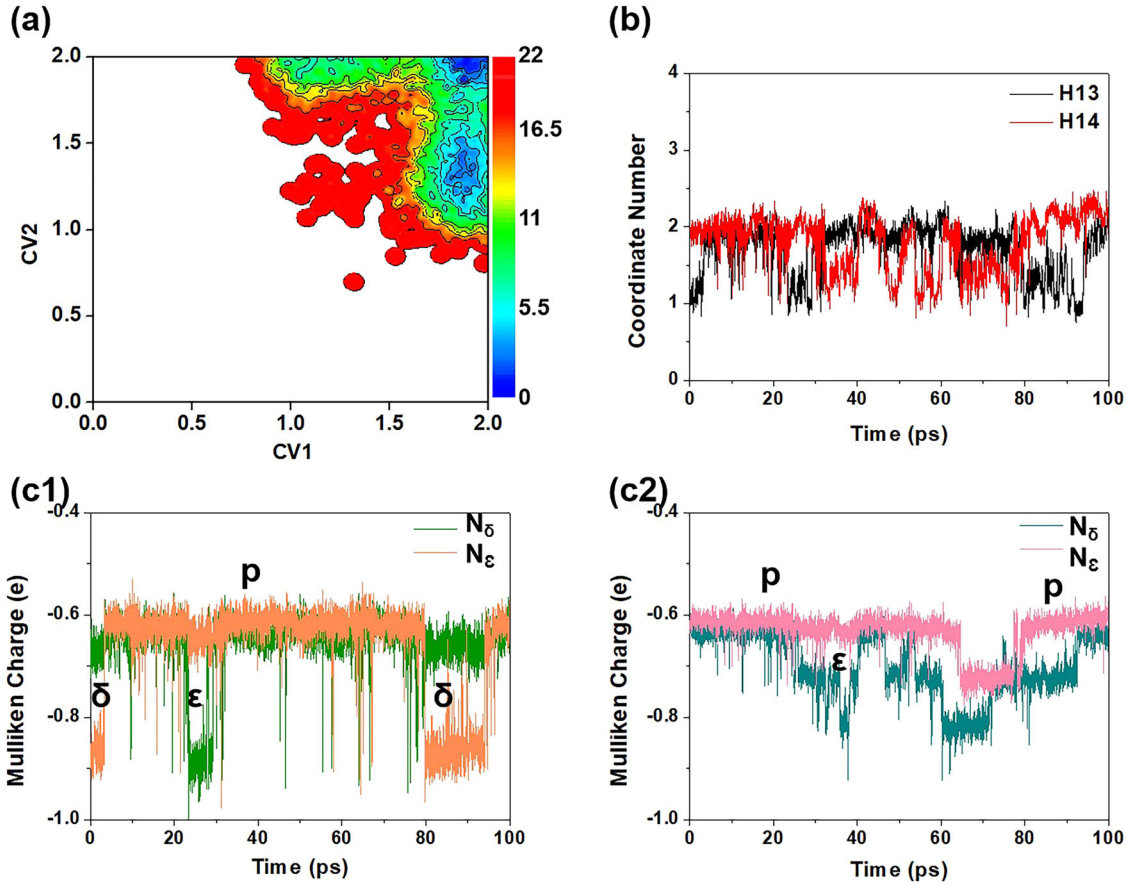

Fig. 5 | FES and electronic evolution of Aβ-40 tautomerization in 2D-WTMTD simulation. a 2D FES in kcal mol^{-1} of the proton transfer process along the CV for the tautomerism between HIS13 and HIS14 of Aβ-40 in the water environment. **b** The H coordination number as a function of 100 ps 2D-WTMTD simulation time. **c1** Functions of Mulliken charge changes of N_δ and N_ε atom on HIS13 and **c2** HIS14 residues as a function with the 100 ps 2D-WTMTD simulation times.

2D-WTMTD simulation as shown in Supplementary Fig. 5. The results in Supplementary Fig. 5 are highly consistent with the findings above, with a proton transfer barrier of ~3.67 kcal mol^{-1}. It further validates the reliability of our results.

To further clarify the specific histidine isomeric form of Aβ-40 within the 15 ps 2D WTMTD simulation, we analyzed the H-coordination numbers of the N atom sites in HIS13 and HIS14, along with the corresponding Mulliken charge variations over time, as shown in Figs. 5b and 4(c1-c2). Snapshots of the proton transfer pathway during the 2D-WTMTD simulation are displayed in Fig. 6, more detailed snapshots are shown in Supplementary Fig. 6, and corresponding Mulliken charge values are presented in Table 1.

As shown in Fig. 6, the initial structure of Aβ-40 and the water molecules retain the (*p, δ*) form and an OH^- ion. Subsequently, the N_ε atom in HIS13 tends to accept a proton from the adjacent water molecules W_1 and W_2, forming the (*p*) form at the HIS13 residue at 3.81 ps. At 23.58 ps, a hydrogen atom is lost from the N_ε site of the HIS13 residue and transferred to the W_7 atom, forming the (*ε, p*) isomer. Subsequently, the N_ε atom in HIS13 recaptures the H atom from W_7, and the hydrogen atom on the N_δ of HIS14 transfers to W_{11}, forming an H_3O^+. This results in the (*p, ε*) configuration at 32.46 ps. At 40.26 ps, the N_δ atom of HIS14 recaptures the hydrogen atom from the water molecule, forming the (*p, p*) configuration. Subsequently, the N_δ atom of HIS14 repeatedly loses and recaptures the hydrogen atom, alternating between the (*p, ε*) and (*p, p*) states until 60.70 ps. At 79.80 ps, the hydrogen atom at the N_ε site of HIS13 donates to W_{10} to form H_3O^+, placing HIS13 in the *δ* state; HIS14 stabilizes in the (*p*) state, resulting in a (*δ, p*) state. However, at 95.12 ps, HIS13 acquires a hydrogen atom from W_{19}, forming a stable (*p, p*) state. It should be noted that many activities of water molecules were not individually described in this process, as they were mutually transferring protons without affecting the interconversion mechanism of HIS13 and HIS14.

Overall, it has been found from the snapshots that HIS13 mainly remains protonated, with a small fraction in the *δ* states, while HIS14 fluctuates between the *p* and *ε* states. This suggests that the most stable configuration of Aβ-40 in the 2D FES is the (*p, p*) tautomer, followed by the (*p, ε*) form, rather than the (*p, δ*) tautomeric form. This indicates that the N_ε atoms of HIS13 and HIS14 have a stronger affinity for accepting protons from the surrounding water molecules than for breaking the N_δ-H bond, resulting in both N atoms on the histidine imidazole ring remaining protonated. Additionally, since the stronger bonding strength of the N_ε-H bond compared to the N_δ-H bond, the (*p, p*) tautomer is the preferred and more stable structure relative to the initial (*δ, δ*) conformation. Previous studies by Nam et al.[42]. reported that the *β*-content in the protonated Aβ-40 monomer is higher than in the *δ* and *ε* conformers, and Chatterjee et al.[50] also demonstrated that the *β*-content in the protonated Aβ-40 homodimer exceeds that of the δ and ε forms. These findings align well with our results, which explain the conformational changes observed between the (*δ, δ*) and (*p, p*) states of Aβ-40.

Conclusions

We have successfully explored the proton transfer mechanism in Aβ-40 tautomers, mediated by water molecules, using a combination of MD and DC-DFTB/MTD simulations. We calculated the proton transfer barrier during the tautomerization process of Aβ-40 tautomers. Our findings, supported by radial distribution functions, free energy surface profiles, H-coordination numbers, and Mulliken charge changes, provide a detailed

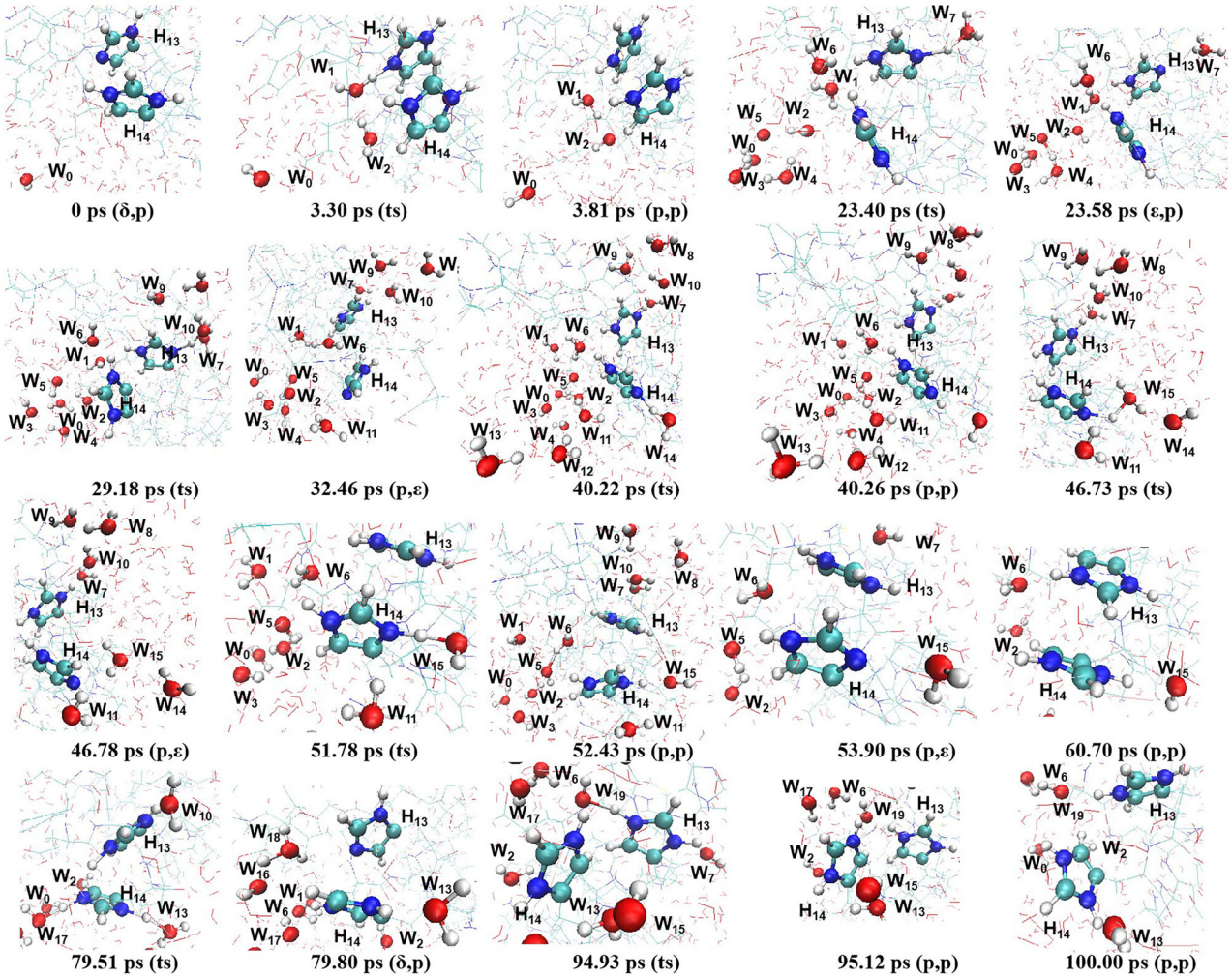

Fig. 6 | Close-up snapshots of the proton transfer pathway from 2D-WTMTD simulation. The snapshots of close-up structures of the proton transfer pathway in 100 ps 2D-WTMTD. The W_n (n = 0-19) was numbered water molecules according to the order of participation in the proton transfer process. (H_{13} and H_{14} are used instead of HIS13 and HIS14, respectively, inside the figure).

understanding of the dynamic proton transfer in Aβ-40 tautomerization. Our MD simulations revealed that the (δ, δ) form of Aβ-40 has the highest β-sheet content among the isomers examined, which plays a crucial role in its structural stability. The DC-DFTB-MD simulations captured a key proton transfer event at the N_ε atom of the HIS13 residue. Moreover, we utilized 2D well-tempered metadynamics and provided a relatively accurate barrier estimate of the proton transfer transition barrier in Aβ-40, ~3.51 kcal mol^{-1}. This work represents a significant advancement in understanding histidine tautomerization in Aβ-40 proteins and establishes a solid theoretical foundation for future studies of Alzheimer's disease pathogenesis. By illuminating the proton transfer dynamics in Aβ-40, our findings offer critical insights into the molecular mechanisms underlying Alzheimer's disease, with the potential to inform future therapeutic strategies targeting Aβ protein. Our study extends beyond earlier computational works that examined His13/His14 tautomerism mainly in the context of secondary-structure stability, dimerization, or metal/ligand interactions. While previous studies showed that these residues influence β-sheet formation and coordinate biometals such as Cu^{2+} and Zn^{2+}, we specifically reveal the proton transfer barrier and mechanism of tautomerization within full Aβ-40 peptides. By quantifying the tautomerization energy landscape, our results complement existing models of dimerization and metal chelation, providing a more comprehensive understanding of the role of His13/His14 in Alzheimer's disease.

Methods

Classical MD simulation

Atomistic Molecular dynamics (MD) simulations were carried out for the aqueous solution of the Aβ40 monomer. The crystal structure (PDB: 1BA4) was obtained from the Protein Data Bank. The four tautomeric isomers, i.e., $\delta\delta$, $\delta\varepsilon$, $\varepsilon\varepsilon$, and $\varepsilon\delta$ tautomers, are prepared by residual substitution with N_δ-H or N_ε-H at the 13 and 14 histidine residues of Aβ 40, and the HIS 6 residue keeps the ε state as the most abundant conformation. The N and C termini were capped with the ACE and NME. MD simulations are performed using the Amber99SB-ILDN force field for protein and the Water molecules were modeled using TIP3P, a model compatible with the Amber99SB-ILDN force field[51,52]. The initial structures in a cubic box are solvated with ~10,000 water molecules (~30,000 atoms) to ensure the natural water density of 0.997 g/cm^3. To eliminate the initial stress, energy minimization was performed before equilibration. The systems were then equilibrated for 2 ns, first in the NVT and subsequently in the NPT ensemble. During the simulation, the temperature was maintained at 300 K using a v-rescale method[53] thermostat with a coupling constant of 1.0 ps^{-1}. The pressure was controlled using the Berendsen barostat with a 2 ps isotropic coupling constant to ensure system stability. Long-range electrostatic interactions were calculated using the particle mesh Ewald (PME) method. Finally, a 200 ns production run was conducted under NPT conditions, ensuring stable trajectories were generated for further analysis. Classical MD

Table 1 | The Mulliken charge of N_δ/N_ε atom of HIS13 and HIS14 residues (unit in *e*)

Simulation Time (ps)	HIS13		HIS14	
	N_δ	N_ε	N_δ	N_ε
0	−0.65	−0.87	−0.61	−0.63
3.30	−0.66	−0.84	−0.62	−0.62
3.81	−0.63	−0.63	−0.65	−0.62
23.40	−0.64	−0.67	−0.62	−0.61
23.58	−0.92	−0.62	−0.64	−0.63
29.18	−0.70	−0.64	−0.68	−0.62
32.46	−0.62	−0.59	−0.91	−0.61
40.22	−0.64	−0.61	−0.68	−0.62
40.26	−0.61	−0.62	−0.64	−0.64
46.73	−0.64	−0.66	−0.90	−0.64
46.78	−0.68	−0.59	−0.94	−0.62
51.78	−0.63	−0.60	−0.69	−0.60
52.43	−0.64	−0.59	−0.70	−0.55
53.90	−0.66	−0.59	−0.95	−0.62
60.70	−0.65	−0.59	−0.65	−0.58
79.51	−0.64	−0.67	−0.66	−0.67
79.80	−0.68	−0.90	−0.66	−0.66
94.93	−0.65	−0.64	−0.67	−0.56
95.12	−0.63	−0.62	−0.67	−0.60
100.00	−0.64	−0.63	−0.61	−0.64

simulations were performed independently for each of the four histidine tautomeric isomers ($\delta\delta$, $\delta\varepsilon$, $\varepsilon\delta$, and $\varepsilon\varepsilon$) to comprehensively sample their conformational behavior. The MD simulations were performed using the Gromacs 2020 package[54–56]. Among the four tautomeric states examined, the $\delta\delta$ isomer was selected as the starting conformation for QM-MD because it exhibited characteristic β-sheet motifs and has been shown to aggregate more frequently than the other configurations, making it a more toxic and biologically relevant state. Representative low-energy snapshots of this $\delta\delta$ isomer were then extracted for subsequent QM-MD simulations. To enhance computational efficiency in the subsequent calculations, the simulated structures of the folding protein system were reduced to 2998 atoms, which were then used as the starting configurations for the following DC-DFTB-MD simulations. For these QM-MD/MTD simulations, we employed the DC-DFTB-MD method, in which the electronic structure is described within the density-functional tight-binding framework, an approximation to Kohn-Sham DFT that reduces computational cost. The divide-and-conquer scheme partitions the system into overlapping subsystems, enabling linear scaling with system size while retaining accuracy in local interactions. This approach is particularly well-suited for biomolecular systems, as it captures essential rare events with quantum mechanical detail while maintaining computational efficiency.

DC-DFTB-MD simulation

The DC-DFTB-MD simulations were performed using the $D_{CDFTBMD}$ program[34,57]. The divide-and-conquer DFTB (DC-DFTB) method was proposed by Yang and co-workers in the 2000s, and is a framework for approximating quantum mechanics (QM) in linear-scaling[58–64], It reduces the computational cost of large-scale DFTB calculations by constructing total density matrix with those of piecewise fragments, followed by computing properties of the whole system from the obtained density matrix. Regarding this specific computational model, Nakai's group designed a program named DC-DFTB-MD, which we applied in this work. It can achieve massive parallelism on scalable supercomputing platforms, and bridging the gap in the scale of QM-based and classical MD simulations. To reduce the boundary errors caused by fragmentation, the DC method introduces a buffer zone containing neighboring atoms for each subsystem when solving the electronic structure, thereby constructing its localized region and maintaining accuracy. All quantum mechanical-based MD simulations were performed at third-order density-functional tight-binding (DFTB3) level. The general 3OB-3-1[65] parameter set for organic and biomolecules, was used for describing the electronic and repulsive parts of the DFTB Hamiltonian. The non-covalent interactions were and characterized by applying Grimme's DFT-D3 dispersion correction with the Becke-Johnson damping scheme[65–69]. The subsystems for the DC scheme were created automatically by defining $3 \times 3 \times 3$ Å^3 cubic grids that slice the overall system. By using this cubic grid, ~1100 subsystems were generated. To compensate for the errors of missing orbital overlaps and atomic interactions, the buffer radius of 6.0 Å was set. The aforementioned DC scheme was initially evaluated by examining the effects of varying the buffer radius and cubic grids on the DFTB total energy. The adopted DC scheme greatly reduces the computational costs and thus enables us to perform large-scale MD simulations. Lagrange interpolation of the Mulliken charge was used to refine the self-consistent charge convergence[70]. The criterion of the self-consistent charge (SCC) convergence was set to 10^{-9} and 10^{-6} au, for the total energy and Mulliken charge, respectively. The soft boundary condition was imposed on the system to avoid water evaporation in long simulations to approach the experiment results. The modified Broyden method was employed as the charge mixing algorithm, with the mixing parameters of 0.3. The structure is equilibrated for 100 ps under the canonical (*NVT*) ensemble. The temperature was maintained at 300 K on the Andersen thermostat. The integrator time step of 0.5 fs was used during the simulations to capture the fast proton transfer event[71].

DC-DFTB-MD/MTD simulation

To investigate the proton transfer process between the HIS13 and HIS14 residues in the Aβ-40 system and to obtain the free energy profiles of histidine tautomerization, DC-DFTB-metadynamics simulations were performed using both a standard scheme and a two-dimensional well-tempered (2D-WT) scheme[72]. In the present work, the two-dimensional well-tempered (2D-WT) was employed to improve the sampling accuracy of the estimated proton transfer barrier, as the standard scheme can potentially lead to oversampling of the deprotonated state, resulting in a hyper stable protonated state. The primary goal of the standard scheme was to verify the observability of the proton transfer using the specified bias potential. The 100 ps standard metadynamics simulation (SMTD) and 15 ps two-dimension well-tempered simulations (2D WTMTD) are performed using the constant value. The collective variables (CVs) were defined as the rational coordination number as shown in Eq. 1

$$\sum_{A\in group1}^{atom}\sum_{B\in group2}^{atom}\frac{1-\left(\frac{r_{AB}}{r_0}\right)^6}{1-\left(\frac{r_{AB}}{r_0}\right)^{12}} \quad (1)$$

Group 1 in Eq.2 consists of four N atoms on the imidazole ring of HIS13 and HIS14 residues, whereas group 2 consists of all H atoms in water molecules and two H atoms in the N_ε-H group of HIS13 and HIS14 residues. The cutoff distance r_0 is 1.4 Å, which was specified to identify the O-H bond cleavage and formation during the metadynamics sampling. The initial Gaussian function for the bias potential was configured to 1.88 kcal mol^{-1}, and the width of the Gauss function is set to $\sigma = 0.02$. The bias factor of 2D WTMTD was set to 14.5, corresponding to the bias temperature of 6600 K. The first and second collective variables (CVs, i.e., CV1 and CV2) are defined as the rational coordination numbers of hydrogen and nitrogen atoms on the imidazole ring of the HIS13 and HIS14 residues. Different random seed numbers of the Andersen thermostat were applied during two rounds of 2D-WTMTD simulations to verify the trends observed in this study. The results of second around 2D-WTMTD simulations are shown in

Supplementary Fig. 5. All structural changes are visualized by using the visual molecular dynamics (VMD) package[73].

Data availability

The data that support the findings of this study are available from the corresponding author upon reasonable request.

Received: 8 April 2025; Accepted: 3 November 2025;
Published online: 11 December 2025

References

1. Nichols, E. et al. Estimation of the global prevalence of dementia in 2019 and forecasted prevalence in 2050: an analysis for the Global Burden of Disease Study 2019. *Lancet Public Health* **7**, e105–e125 (2022).
2. Alzheimer's Association. 2019 Alzheimer's disease facts and figures. *Alzheimer's Dement.* **15**, 321–387 (2019).
3. Rosales-Corral, S. A. et al. Alzheimer's disease: pathological mechanisms and the beneficial role of melatonin. *J. Pineal Res.* **52**, 167–202 (2012).
4. Ju, Y. & Tam, K. Y. Pathological mechanisms and therapeutic strategies for Alzheimer's disease. *Neural Regen. Res.* **17**, 543–549 (2022).
5. Bai, R., Guo, J., Ye, X.-Y., Xie, Y. & Xie, T. Oxidative stress: the core pathogenesis and mechanism of Alzheimer's disease. *Ageing Res. Rev.* **77**, 101619 (2022).
6. Morris, G. P., Clark, I. A. & Vissel, B. Inconsistencies and controversies surrounding the amyloid hypothesis of Alzheimer's disease. *Acta Neuropathol. Commun.* **2**, 1–21 (2014).
7. Liu, P.-P., Xie, Y., Meng, X.-Y. & Kang, J.-S. History and progress of hypotheses and clinical trials for Alzheimer's disease. *Signal Transduct. Target. Ther.* **4**, 29 (2019).
8. Alonso, A.dC., Zaidi, T., Novak, M., Grundke-Iqbal, I. & Iqbal, K. Hyperphosphorylation induces self-assembly of τ into tangles of paired helical filaments/straight filaments. *Proc. Natl. Acad. Sci. USA* **98**, 6923–6928 (2001).
9. Hardy, J. & Selkoe, D. J. The amyloid hypothesis of Alzheimer's disease: progress and problems on the road to therapeutics. *Science* **297**, 353–356 (2002).
10. Santos, M. A., Chand, K. & Chaves, S. Recent progress in multifunctional metal chelators as potential drugs for Alzheimer's disease. *Coord. Chem. Rev.* **327-328**, 287–303 (2016).
11. Chaves, S., Várnagy, K. & Santos, M. A. Recent multi-target approaches on the development of anti-Alzheimer's agents integrating metal chelation activity. *Curr. Med. Chem.* **28**, 7247–7277 (2021).
12. Stefanachi, A., Leonetti, F., Pisani, L., Catto, M. & Carotti, A. Coumarin: a natural, privileged and versatile scaffold for bioactive compounds. *Molecules* **23**, 250 (2018).
13. Shankar, G. M. et al. Amyloid β-protein dimers isolated directly from Alzheimer brains impair synaptic plasticity and memory. *Nat. Med.* **14**, 837 (2008).
14. Goure, W. F., Krafft, G. A., Jerecic, J. & Hefti, F. Targeting the proper amyloid-beta neuronal toxins: a path forward for Alzheimer's disease immunotherapeutics. *Alzheimers Res. Ther.* **6**, 1–15 (2014).
15. Itoh, S. G., Yagi-Utsumi, M., Kato, K. & Okumura, H. Key residue for aggregation of amyloid-β peptides. *ACS Chem. Neurosci.* **13**, 3139–3151 (2022).
16. Tsigelny, I. F. et al. Structural diversity of Alzheimer's disease Aβ Dimers and their role in oligomerization and fibril formation. *J. Alzheimers Dis.* **39**, 583 (2014).
17. Puentes-Díaz, N., Chaparro, D., Morales-Morales, D., Flores-Gaspar, A. & Alí-Torres, J. Role of metal cations of copper, iron, and aluminum and multifunctional ligands in Alzheimer's disease: experimental and computational insights. *ACS Omega* **8**, 4508–4526 (2023).
18. Lv, Z., Roychaudhuri, R., Condron, M. M., Teplow, D. B. & Lyubchenko, Y. L. Mechanism of amyloid Β-protein dimerization determined using single−molecule AFM force spectroscopy. *Sci. Rep.* **3**, 1–8 (2013).
19. Müller-Schiffmann, A. et al. Amyloid-β dimers in the absence of plaque pathology impair learning and synaptic plasticity. *Brain* **139**, 509–525 (2016).
20. Beck, M. W. et al. Structure-mechanism-based engineering of chemical regulators targeting distinct pathological factors in Alzheimer's disease. *Nat. Commun.* **7**, 13115 (2016).
21. Kepp, K. P. Bioinorganic chemistry of Alzheimer's disease. *Chem. Rev.* **112**, 5193–5239 (2012).
22. Zhang, C.-E. et al. Hyperhomocysteinemia increases β-amyloid by enhancing expression of γ-secretase and phosphorylation of amyloid precursor protein in rat brain. *Am. J. Pathol.* **174**, 1481–1491 (2009).
23. Zhang, R., Ai, H., Zhu, X. & Li, Q. Molecular simulations of human and mouse Aβ1–16 at different pH values: structural characteristics toward understanding Cu2+-coordinated amyloid beta spheres. *ChemPhysChem* **17**, 1656–1668 (2016).
24. Shi, H. & Lee, J. Y. Tautomeric effect of histidine on the monomeric structure of amyloid β-peptide (1–42). *ACS Chem. Neurosci.* **8**, 669–675 (2017).
25. Shi, H., Kang, B. & Lee, J. Y. Tautomeric effect of histidine on the monomeric structure of amyloid β-peptide (1–40). *J. Phys. Chem. B.* **120**, 11405–11411 (2016).
26. Parnetti, L. et al. Performance of Aβ 1-40, Aβ 1-42, total tau, and phosphorylated tau as predictors of dementia in a cohort of patients with mild cognitive impairment. *J. Alzheimer's Dis.* **29**, 229–238 (2012).
27. Zou, K. et al. Amyloid β-protein (Aβ) 1–40 protects neurons from damage induced by Aβ1–42 in culture and in rat brain. *J. Neurochem.,* **87**, 609–619 (2003).
28. Goldsbury, C. S. et al. Studies on the in vitro assembly of Aβ 1–40: implications for the search for Aβ fibril formation inhibitors. *J. Struct. Biol.* **130**, 217–231 (2000).
29. Salimi, A., Li, H., Shi, H. & Lee, J. Y. Intrinsic origin of amyloid aggregation: behavior of histidine (εεε) and (δδδ) tautomer homodimers of Aβ (1–40). *Biochim. Biophys. Acta Gen. Subj.* **1863**, 795–801 (2019).
30. Parida, R., Rafiq, F., Chatterjee, S., Salimi, A., Yong Lee, J. Insights into amyloid-β misfolding: The impact of histidine tautomerism and Au(111) surfaces through MD simulations and 2DIR spectroscopy. *Int. J. Biol. Macromol*. **312**, 144098 (2025).
31. Tang, Y., Li, N., Li, H., Li, H. & Lee, J. Y. Probing the water-mediated proton transfer in histidine tautomerization. *J. Mol. Liq.* **387**, 122639 (2023).
32. Falvo, C. et al. Frequency distribution of the amide-I vibration sorted by residues in amyloid fibrils revealed by 2D-IR measurements and simulations. *J. Phys. Chem. B.* **116**, 3322–3330 (2012).
33. Ono, J., Imai, M., Nishimura, Y. & Nakai, H. Hydroxide ion carrier for proton pumps in bacteriorhodopsin: primary proton transfer. *J. Phys. Chem. B.* **124**, 8524–8539 (2020).
34. Nishimura, Y. & Nakai, H. Dcdftbmd: divide-and-conquer density functional tight-binding program for huge-system quantum mechanical molecular dynamics simulations. *J. Comput. Chem.* **40**, 1538–1549 (2019).
35. Nakai, H., Takemura, T., Ono, J. & Nishimura, Y. Quantum-mechanical molecular dynamics simulations on secondary proton transfer in bacteriorhodopsin using realistic models. *J. Phys. Chem. B.* **125**, 10947–10963 (2021).
36. Ono, J., Okada, C. & Nakai, H. Hydroxide Ion mechanism for long-range proton pumping in the third proton transfer of bacteriorhodopsin. *ChemPhysChem* **23**, e202200109 (2022).

37. Nishimura, Y. & Nakai, H. Hierarchical parallelization of divide-and-conquer density functional tight-binding molecular dynamics and metadynamics simulations. *J. Comput. Chem.* **41**, 1759–1772 (2020).
38. Sakti, A. W., Nishimura, Y. & Nakai, H. Recent advances in quantum-mechanical molecular dynamics simulations of proton transfer mechanism in various water-based environments. *Wiley Interdiscip. Rev. Comput. Mol. Sci.* **10**, e1419 (2020).
39. Schrödinger, E. Quantisierung als eigenwertproblem. *Ann. Phys.* **385**, 437–490 (1926).
40. Slocombe, L., Sacchi, M. & Al-Khalili, J. An open quantum systems approach to proton tunnelling in DNA. *Commun. Phys.* **5**, 109 (2022).
41. Mori, Y. & Okamoto, Y. Free-energy analyses of a proton transfer reaction by simulated-tempering umbrella sampling and first-principles molecular dynamics simulations. *Phys. Rev. E.* **87**, 023301 (2013).
42. Nam, Y., Kalathingal, M., Saito, S. & Lee, J. Y. Tautomeric effect of histidine on β-Sheet formation of amyloid beta 1–40: 2D-IR simulations. *Biophys. J.* **119**, 831–842 (2020).
43. Passarella, D. & Goedert, M. Beta-sheet assembly of Tau and neurodegeneration in Drosophila melanogaster. *Neurobiol. Aging* **72**, 98–105 (2018).
44. Lovestone, S. & McLoughlin, D. Protein aggregates and dementia: is there a common toxicity? *J. Neurol. Neurosurg. Psychiatry* **72**, 152–161 (2002).
45. Marsili, S., Barducci, A., Chelli, R., Procacci, P. & Schettino, V. Self-healing umbrella sampling: a non-equilibrium approach for quantitative free energy calculations. *J. Phys. Chem. B.* **110**, 14011–14013 (2006).
46. Dickson, B. M., Legoll, F., Lelievre, T., Stoltz, G. & Fleurat-Lessard, P. Free energy calculations: an efficient adaptive biasing potential method. *J. Phys. Chem. B.* **114**, 5823–5830 (2010).
47. Bilionis, I. & Koutsourelakis, P.-S. Free energy computations by minimization of Kullback–Leibler divergence: an efficient adaptive biasing potential method for sparse representations. *J. Comput. Phys.* **231**, 3849–3870 (2012).
48. Bussi, G., Laio, A. & Parrinello, M. Equilibrium free energies from nonequilibrium metadynamics. *Phys. Rev. Lett.* **96**, 090601 (2006).
49. Tribello, G. A., Ceriotti, M. & Parrinello, M. A self-learning algorithm for biased molecular dynamics. *Proc. Natl Acad. Sci. Usa.* **107**, 17509–17514 (2010).
50. Chatterjee, S., Nam, Y., Salimi, A. & Lee, J. Y. Monitoring early-stage β-amyloid dimer aggregation by histidine site-specific two-dimensional infrared spectroscopy in a simulation study. *Phys. Chem. Chem. Phys.* **24**, 18691–18702 (2022).
51. Lindorff-Larsen, K. et al. Improved side-chain torsion potentials for the Amber ff99SB protein force field. *Proteins: Struct., Funct., Bioinforma.* **78**, 1950–1958 (2010).
52. Jorgensen, W. L., Chandrasekhar, J., Madura, J. D., Impey, R. W. & Klein, M. L. Comparison of simple potential functions for simulating liquid water. *J. Chem. Phys.* **79**, 926–935 (1983).
53. Bussi, G., Donadio, D. & Parrinello, M. Canonical sampling through velocity rescaling. *J. Chem. Phys.* **126**, 014101 (2007).
54. Bekker, H. et al. In *Gromacs-a Parallel Computer for Molecular-Dynamics Simulations*, 4th international conference on computational physics (PC 92) 252–256 (World Scientific Publishing, 1993).
55. Berendsen, H. J., van der Spoel, D. & van Drunen, R. GROMACS: a message-passing parallel molecular dynamics implementation. *Comput. Phys. Commun.* **91**, 43–56 (1995).
56. Abraham, M. J. et al. GROMACS: high-performance molecular simulations through multi-level parallelism from laptops to supercomputers. *SoftwareX* **1**, 19–25 (2015).
57. DCDFTBMD, accessed 20 August 2021. http://www.chem.waseda.ac.jp/dcdftbmd/.
58. Yang, W. Direct calculation of electron density in density-functional theory. *Phys. Rev. Lett.* **66**, 1438 (1991).
59. Yang, W. & Lee, T.-S. A density-matrix divide-and-conquer approach for electronic structure calculations of large molecules. *J. Chem. Phys.* **103**, 5674 (1995).
60. Kobayashi, M. & Nakai, H. *Linear-Scaling Techniques in Computational Chemistry and Physics* (eds Zalesny, R., Papadopoulos, M. G., Mezey, P. G., Leszczynski, J.) 97–127 (Springer, 2011).
61. Kobayashi, M. & Nakai, H. How does it become possible to treat delocalized and/or open-shell systems in fragmentation-based linear-scaling electronic structure calculations? The case of the divide-and-conquer method. *Phys. Chem. Chem. Phys.* **14**, 7629 (2012).
62. Liu, H. et al. Quantum mechanics simulation of protein dynamics on long timescale. *Proteins* **44**, 484 (2001).
63. Lu, Z., Nowak, W., Lee, G., Marszalek, P. E. & Yang, W. Elastic properties of single amylose chains in water: a quantum mechanical and AFM study. *J. Am. Chem. Soc.* **126**, 9033 (2004).
64. Hu, H., Lu, Z., Elstner, M., Hermans, J. & Yang, W. Simulating water with the self-consistent-charge density functional tight binding method: from molecular clusters to the liquid state. *J. Phys. Chem. A.* **111**, 5685 (2007).
65. Gaus, M., Goez, A. & Elstner, M. Parametrization and benchmark of DFTB3 for organic molecules. *J. Chem. Theory Comput.* **9**, 338–354 (2013).
66. Gaus, M., Lu, X., Elstner, M. & Cui, Q. Parameterization of DFTB3/3OB for sulfur and phosphorus for chemical and biological applications. *J. Chem. Theory Comput.* **10**, 1518–1537 (2014).
67. Kubillus, M., Kubar, T., Gaus, M., Rezac, J. & Elstner, M. Parameterization of the DFTB3 method for Br, Ca, Cl, F, I, K, and Na in organic and biological systems. *J. Chem. Theory Comput* **11**, 332–342 (2015).
68. Grimme, S., Antony, J., Ehrlich, S. & Krieg, H. A consistent and accurate ab initio parametrization of density functional dispersion correction (DFT-D) for the 94 elements H-Pu. *J. Chem. Phys.* **132**, 154104 (2010).
69. Grimme, S., Ehrlich, S. & Goerigk, L. Effect of the damping function in dispersion corrected density functional theory. *J. Comput. Chem.* **32**, 1456–1465 (2011).
70. Atsumi, T. & Nakai, H. Molecular orbital propagation to accelerate self-consistent-field convergence in an ab initio molecular dynamics simulation. *J. Chem. Phys.* **128**, 094101 (2008).
71. Andersen, H. C. Molecular dynamics simulations at constant pressure and/or temperature. *J. Chem. Phys.* **72**, 2384–2393 (1980).
72. Barducci, A., Bussi, G. & Parrinello, M. Well-tempered metadynamics: a smoothly converging and tunable free-energy method. *Phys. Rev. Lett.* **100**, 020603 (2008).
73. Humphrey, W., Dalke, A. & Schulten, K. VMD: visual molecular dynamics. *J. Mol. Graph.* **14**, 33–38 (1996).

Acknowledgements

This work was supported by the National Research Foundation of Korea (NRF) grant funded by the Korean government (MSIT) (No. NRF-2021R1A2C2095412 & NRF-2022R1A2C1092044).

Author contributions

Y.T. idea, conceptualization, investigation, data analysis, writing—original draft; Y.N. methodology, investigation, data curation, validation; N.L. data analysis, writing—original draft; H.L. methodology, formal analysis, visualization; A.S. methodology, formal analysis; K.I. methodology, investigation; A.W.S. methodology, validation, investigation; H.N. methodology, software, resources, supervision; R.P. visualization, writing—original draft, investigation; J.Y.L. conceptualization, writing—review and editing, supervision, project administration.

Competing interests

The authors declare no competing interests.

Additional information

Supplementary information The online version contains supplementary material available at https://doi.org/10.1038/s42004-025-01790-x.

Correspondence and requests for materials should be addressed to Aditya Wibawa Sakti, Hiromi Nakai, Rakesh Parida or Jin Yong Lee.

Peer review information *Communications Chemistry* thanks the anonymous reviewers for their contribution to the peer review of this work. A peer review file is available.